Nondegenerate Parametric Resonance in Large Ensembles of Coupled Micromechanical Cantilevers with Varying Natural Frequencies

Christopher B. Wallin,[1,2] Roberto De Alba,[1,2] Daron Westly,[1] Glenn Holland,[1] Scott Grutzik,[3] Richard H. Rand,[4,5]
Alan T. Zehnder,[4] Vladimir A. Aksyuk,[1] Slava Krylov,[6] and B. Robert Ilic[1,*]
[1]*Physical Measurement Laboratory, National Institute of Standards and Technology, Gaithersburg, Maryland 20899, USA*
[2]*Institute for Research in Electronics and Applied Physics, University of Maryland, College Park, Maryland 20742, USA*
[3]*Component Science and Mechanics, Sandia National Laboratories, Albuquerque, New Mexico 87185, USA*
[4]*Sibley School of Mechanical and Aerospace Engineering, Cornell University, Ithaca, New York 14853, USA*
[5]*Department of Mathematics, Cornell University, Ithaca, New York 14853, USA*
[6]*School of Mechanical Engineering, Faculty of Engineering, Tel Aviv University, Ramat Aviv 69978, Tel Aviv, Israel*

(Received 10 July 2018; published 28 December 2018)

We investigate the collective dynamics and nondegenerate parametric resonance (NPR) of coplanar, interdigitated arrays of microcantilevers distinguished by their cantilevers having linearly expanding lengths and thus varying natural frequencies. Within a certain excitation frequency range, the resonators begin oscillating via NPR across the entire array consisting of 200 single-crystal silicon cantilevers. Tunable coupling generated from fringing electrostatic fields provides a mechanism to vary the scope of the NPR. Our experimental results are supported by a reduced-order model that reproduces the leading features of our data including the NPR band. The potential for tailoring the coupled response of suspended mechanical structures using NPR presents new possibilities in mass, force, and energy sensing applications, energy harvesting devices, and optomechanical systems.

DOI: 10.1103/PhysRevLett.121.264301

With the emergence of micro and nanoelectromechanical systems (M/NEMS) in recent decades, M/NEMS resonator arrays have been increasingly employed in the practical study of the complex, collective behavior of coupled oscillator systems. Large arrays of coupled microelectromechanical resonators were first reported in the seminal work of Buks and Roukes [1], whereby 67 electrostatically coupled, doubly clamped beams produced rather unanticipated responses. Instead of featuring 67 collective vibrational modes, their nonlinear responses exhibited a small number of asymmetric resonance peaks, which were broad relative to the expected mode spacing, extended beyond their predicted band edges, and displayed abrupt pattern switching behavior. Subsequently, M/NEMS resonator arrays have been shown to exhibit a host of nontrivial dynamics due predominantly to their nonlinear nature including intrinsically localized modes [2–4], multistability and hysteresis [5], and synchronization [6–8]. The applicability of these M/NEMS resonator arrays also has been wide ranging and includes signal processing applications such as radio frequency filtering [9] and frequency conversion [10], oscillator phase noise reduction through synchronization for enhanced clocking and frequency stability [11–14], and ultrasensitive mode-localized sensing [15–18]. Many of these effects and their derived applications fundamentally depend on the complicated interplay between various constituents of the array due to coupling mechanisms which are generally mediated elastically [19–21], optically [22–24], or electrostatically [1,25–27]. Although theoretical investigations into large degree of freedom resonator arrays commonly focus on the system's response to changes in coupling parameters and natural frequencies [6,28–30], experimental implementation of such devices remains challenging because they usually require complicated coupling topologies and complex readout transduction schemes. Nonetheless, device realization of globally tunable coupled array systems is relatively straightforward, especially with electrostatic coupling which does not necessitate additional piezoelectric or optical device layers.

Customarily, the electrostatic coupling or drive configurations in M/NEMS naturally give rise to parametric excitation and resonance through time-dependent, nonlinear electrostatic forces which effectively create modulating spring constants. Utilizing electrostatic parametric resonance in M/NEMS has become ubiquitous principally due to its capability of producing resonant responses when excited at frequencies other than at the system's natural frequency, along with the ease of implementation. These systems are routinely described by a generalization of Mathieu's equation, namely the nonlinear Hill's equation. It is well known that Mathieu's equation has parametric instability tongues that exist near frequencies $f = 2f_j^{NM}/k$ where f_j^{NM} is a jth natural frequency of the system, $k = 1, 2, \ldots$, and the superscript NM denotes a normal mode [31]. These critical frequency values represent fundamental parametric resonance of order k and have been explored in M/NEMS for reasonably high values of k despite the fact that higher-order resonances progressively have exponential narrowing of their instability regions [32,33].

Further possibilities of parametric resonance exist in multidegree of freedom systems where the possibility of mutual interaction of eigenmodes exists. Nondegenerate parametric resonance (NPR), also known as combination parametric resonance [31], occurs in neighborhoods near frequency values $f \approx (f_j^{NM} \pm f_l^{NM})/k$ for $j, l = 1, 2, \ldots$ and $k = 1, 2, \ldots$ where f_j^{NM} and f_l^{NM} correspond to distinct normal modes of the system. In general, NPR emerges in systems with time-dependent mode couplings, which result in frequency mixing and parametric resonant responses at sums or differences of the system's natural frequencies. Although NPR has been well studied theoretically [31,34,35], actual implementation of NPR in M/NEMS has been limited [36–41] and has not been observed in large M/NEMS arrays to the best of our knowledge.

In this Letter, we consider both theoretically and experimentally the complex behavior and NPR of coupled, parametrically driven, interdigitated arrays of microcantilevers with linearly changing cantilever lengths. More specifically, we describe herein the array-spanning, summed-type NPR that occurs over a wide frequency band due to the distinctive spatially confined mode structure and the associated natural frequency distribution resulting from the geometry of the device.

As shown in Fig. 1(a), the device is composed of two opposing, partially interdigitated cantilever arrays with 100 cantilevers apiece. Each array has cantilever lengths expanding linearly across the device in opposite directions with a maximum length of $L_{\max} \approx 500\ \mu$m and a minimum length of $L_{\min} \approx 350\ \mu$m. The width and thickness of the cantilevers are $b \approx 20\ \mu$m and $h \approx 5\ \mu$m, respectively. Additional device parameters include the gap length between neighboring counter-orientated cantilevers, the length of the compliant overhang, and the length of the overlap region. These parameters, respectively, correspond to $g \approx 5\ \mu$m, $L_o \approx 100\ \mu$m, and $L_e \approx 150\ \mu$m. Fabrication process details can be found in Ref. [42].

In the overlap region, electrostatic coupling is generated through the asymmetries in the fringing fields between neighboring cantilevers and serves to produce an electrostatic restoring force as illustrated in Fig. 1(b). The electrostatic

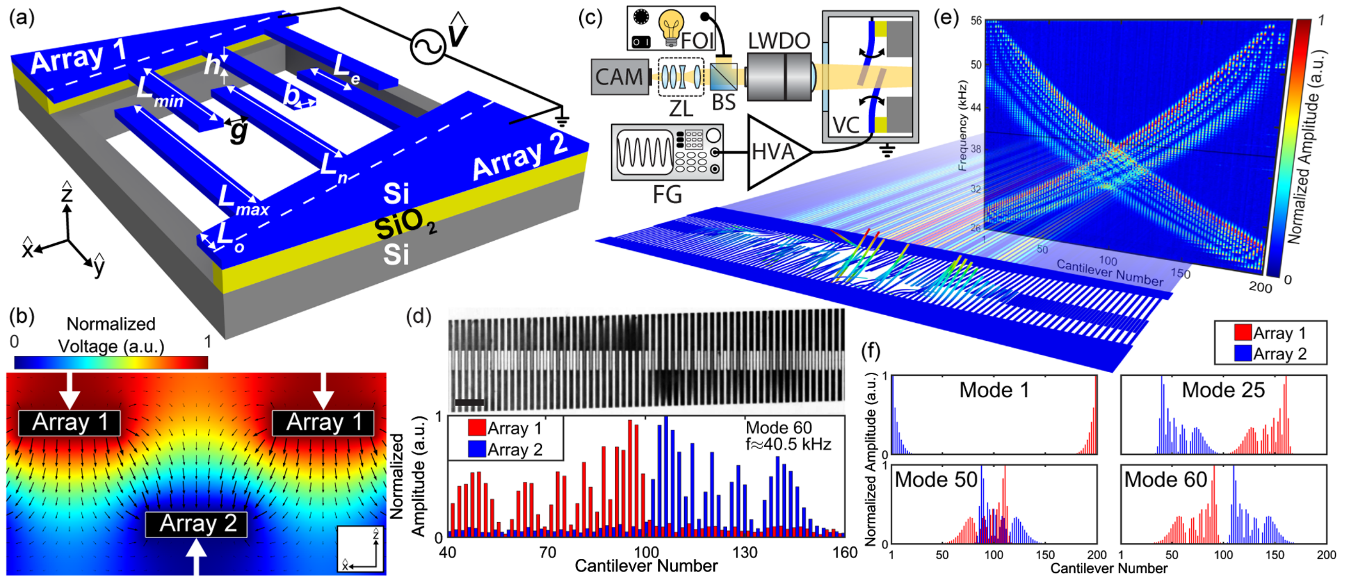

FIG. 1. (a) Schematic of the interdigitated, variable length microcantilever arrays. The actual device has 200 cantilevers. Electrostatic coupling between oppositely oriented, nearest-neighbor cantilevers is generated via fringing electrostatic fields in the overlap region designated by L_e. Long-range mechanical coupling is produced in each array's overhang, which is defined by L_o and delineated by the dashed lines on array 1 and array 2. (b) Results from finite element (FE) analysis illustrating the fringing electrostatic field between adjacent cantilevers in the overlap region. This field provides a restoring force between neighboring beams as indicated by the white arrows. The lengths of the black arrows are proportional to the electric field strength at the given locations. (c) Schematic of the experimental setup. (d) An optical micrograph (top) of the center of the device being actuated at a drive frequency of $f_D \approx 40.5$ kHz. The scale bar is 100 μm. The spatially averaged grayscale pixel values (bottom) are obtained from the end of each cantilever providing a qualitative estimate of the out-of-plane vibrational amplitude for every cantilever on the device. (e) Modal patterns are developed by concatenating together the response at each frequency step [26]. The rendered image of a device consisting of 200 oscillating cantilevers shows explicitly the mapping of the device dynamics at $f_D \approx 40.5$ kHz to an experimentally obtained modal pattern. For the sake of clarity of the mapping, the experimental modal pattern was specifically chosen to consist only of the normal modes of the system and to exhibit no NPR. (f) Normalized amplitudes of various spatially localized modes generated from a full-scale FE modal analysis [43]. Spatial overlap of the opposing arrays' modes is a necessary condition for NPR excitation in the system.

force per unit length in the overlap region defined by $L_n - L_e \leq \hat{y} \leq L_n$, acting on the nth cantilever, $F_n^e(\hat{y}, \hat{t})$, can be approximated by Ref. [42] as

$$F_n^e = \alpha\sigma\hat{V}^2\left(\frac{\frac{\hat{w}_{n+1}-\hat{w}_n}{h}}{1+\sigma|\frac{\hat{w}_{n+1}-\hat{w}_n}{h}|^{2p}} - \frac{\frac{\hat{w}_n-\hat{w}_{n-1}}{h}}{1+\sigma|\frac{\hat{w}_n-\hat{w}_{n-1}}{h}|^{2p}}\right), \qquad (1)$$

where $\hat{w}_n(\hat{y})$ is the out-of-plane defection of the nth beam and $\hat{V}(\hat{t})$ is the time-dependent voltage applied across the arrays. The remaining terms, α, σ, and p, are geometry-dependent fitting parameters which were found to be $\alpha = 2.45 \times 10^{-6}$ N mV^{-2}, $\sigma = 0.133$, and $p = 1.191$. In order to motivate the possibility of NPR actuation within the device, further examination of Eq. (1) is necessary. Assuming $\hat{V}(\hat{t}) = \hat{V}_{ac}\cos(\omega_D\hat{t})$ where ω_D is the excitation angular frequency, we find after linearizing Eq. (1) that the electrostatic force per unit length can be approximated by

$$F_n^e \approx \frac{\alpha\sigma}{h}\frac{\hat{V}_{ac}^2}{2}(1 + 2\cos(2\omega_D\hat{t}))(\hat{w}_{n+1} - 2\hat{w}_n + \hat{w}_{n-1}). \qquad (2)$$

Equation (2) represents a coupled Mathieu-type term [31] that produces kth order NPR excitation at critical NPR frequencies $f = 2f_D \approx (f_j^{NM} + f_l^{NM})/k$.

In order to experimentally investigate the dynamics of the arrays, the devices were fixed on a stage in a vacuum chamber (VC) at pressure of $\approx 10^{-3}$ Pa as depicted in Fig. 1(c). The out-of-plane motion of the cantilevers was observed using an optical setup consisting of a 1× long working distance objective (LWDO), a fiber-optic illuminator (FOI), a beam splitter (BS), a zoom lens (ZL), and a camera (CAM). Each measurement involved applying a time-varying voltage undergoing a linearly chirped frequency sweep given by $\hat{V}(\hat{t}) = \hat{V}_{ac}\cos[2\pi(f_0\hat{t} \pm k\hat{t}^2/2)]$ to one array while grounding the opposing array. This time-varying voltage was produced by a function generator (FG) and a high voltage amplifier (HVA). With f_0 being the starting chirp frequency, the drive signal was either up-chirped or down-chirped over a range of ≈ 26 to ≈ 56 kHz at a rate of $k \approx 107$ Hz/s. Because the camera has a frame rate of ≈ 30 s^{-1}, the measurement technique only gives a qualitative estimate to the magnitude of a beam's deflection time averaged over many oscillation periods. As Fig. 1(d) highlights, large cantilever deflections scatter light more readily, leaving their image noticeably darker relative to nonoscillating cantilevers. The estimated vibrational amplitude of each cantilever was determined by the associated grayscale pixel values at the ends of the beams. Pixel averaging was performed over 20 pixels to reduce the noise in the measurement, and background subtraction was performed to reduce errors caused by nonuniform illumination of the sample. Modal pattern maps were generated by obtaining the grayscale pixel values from each video frame and concatenating them together across frequency space, as Fig. 1(e) exemplifies. These experimental modal patterns shown in Fig. 1(e) primarily resemble the normal mode shapes predicted by FE analysis as presented in Fig. 1(f).

While the measurement technique described above is straightforward and provides qualitative estimates for the normal mode shapes and relative vibrational amplitudes, a consequential drawback of its simplicity is that it only gives the system's response at a specified drive frequency and provides no direct measurement of the oscillation frequency of the individual cantilevers. Experimental verification of first-order NPR actuation in the arrays requires that the first-order NPR frequency condition, $f_D \approx (f_j^{NM} + f_l^{NM})/2$, be satisfied and appropriately measured, which is a challenging proposition considering our limited frequency measurement capabilities. In order to circumvent this difficulty, the measured NPR mode shapes were cross-correlated with the measured normal mode shapes. Assuming that the normal modes oscillate at the drive frequency, this procedure gives an estimate of the frequency response of the NPR modes. As shown in Figs. 2(a) and 2(b), the down-chirped response at $\hat{V}_{ac} \approx 40$ V produced 15 distinct NPR modes, which are highlighted in the insets. The normal modes responsible for these excited NPR modes were determined by finding the region within the modal pattern map which gave the maximum two-dimensional cross-correlation with a given NPR mode in a specified array. The analysis was performed across the entire frequency space outside of the NPR band and was subject to the constraint that the cantilevers remain aligned to themselves. As an example of the results obtained from the described procedure, Figs. 2(c)–2(h) show the strong similarity between NPR mode 8 and the matching normal modes.

With the NPR-generating normal modes identified, cantilever-averaged resonance curves were used to find the peak resonant frequencies of the jth normal mode in array 1, $f_j^{NM,1}$, and the lth normal mode in array 2, $f_l^{NM,2}$. Additionally, the peak resonant frequencies of the mth NPR mode for array 1, $f_m^{NPR,1}$, and array 2, $f_m^{NPR,2}$, were found for their respective cantilever-averaged resonance curves. These frequencies, $f_m^{NPR,1}$ and $f_m^{NPR,2}$, are not the oscillation frequency of the NPR modes, but the drive frequency at which the NPR modes have peak resonance. All peak locations were determined by fitting a localized quadratic polynomial using the method of least squares. As shown in Fig. 2(i), the frequency deviation from the NPR frequency condition was calculated by $\Delta f = f_j^{NM,1} + f_l^{NM,2} - 2f_D$, where we have taken $f_D = (f_m^{NPR,1} + f_m^{NPR,2})/2$ to be the drive frequency averaged about the NPR peak resonances in both of the arrays. The maximum observed frequency deviation from the ideal NPR frequency condition for all the modes was less than 15 Hz, which conclusively demonstrates that the modes were excited via the NPR mechanism.

Additional experiments were performed at higher voltages to explore the effects of the nonlinearities and the expanded parametric instability regions produced from the stronger

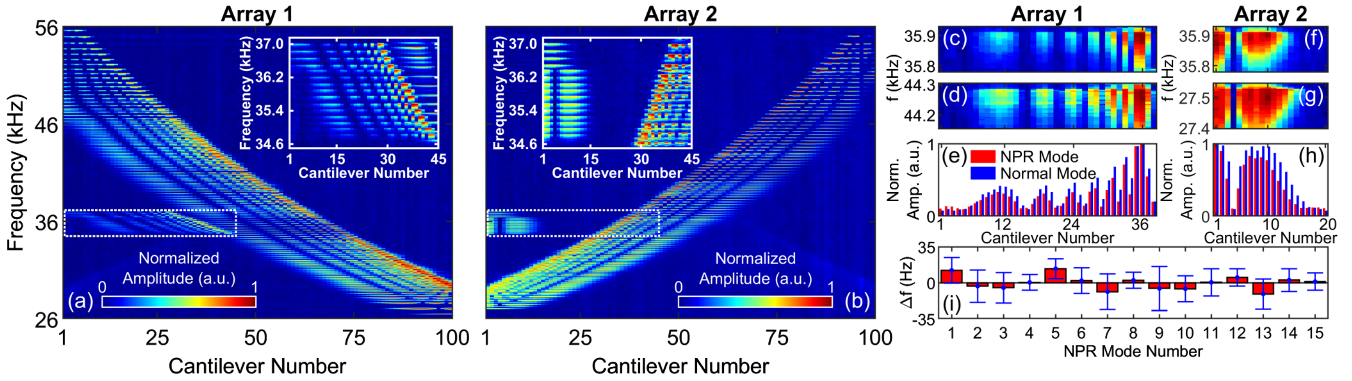

FIG. 2. The frequency response and NPR excitation of (a) array 1 and (b) array 2 driven at $\hat{V}_{ac} \approx 40$ V, which is marginally above the NPR threshold voltage. The 15 observed NPR modes are featured within the dotted rectangles and are replotted in their respective insets. As an example of the results obtained from the normal mode matching algorithm, we have (c) NPR mode 8 and (d) the maximally correlated normal mode, both from array 1, showing almost indistinguishable mode structures. (e) Modal shapes produced by summing over frequency space using array 1's NPR mode 8 and its maximally correlated normal mode, further indicating nearly identical features. (f) NPR mode 8, (g) the maximally correlated normal mode, and (h) the modal shapes, all from array 2, illustrating strong similarity between the two modes. (i) The frequency deviation, Δf, from the NPR frequency condition conclusively demonstrates that the 15 modes outlined above are excited via the NPR mechanism. The error bars correspond to 95% confidence intervals. All plots involving normalized amplitudes are normalized independently.

coupling constant. Figure 3 shows the frequency response at $\hat{V}_{ac} \approx 56$ V and $\hat{V}_{ac} \approx 81$ V using a down-chirped drive. At $\hat{V}_{ac} \approx 56$ V, many NPR modes were actuated, especially along the periphery of the device, as the critical coupling strength was achieved for parametric instability. As the drive voltage was increased to $\approx$81 V, a well-defined NPR band from $\approx$34 to $\approx$ 44 kHz formed and nearly all the cantilevers were oscillating to some degree. The extent of the NPR actuation directly depended on the applied voltage, which is consistent with Eqs. (1) and (2).

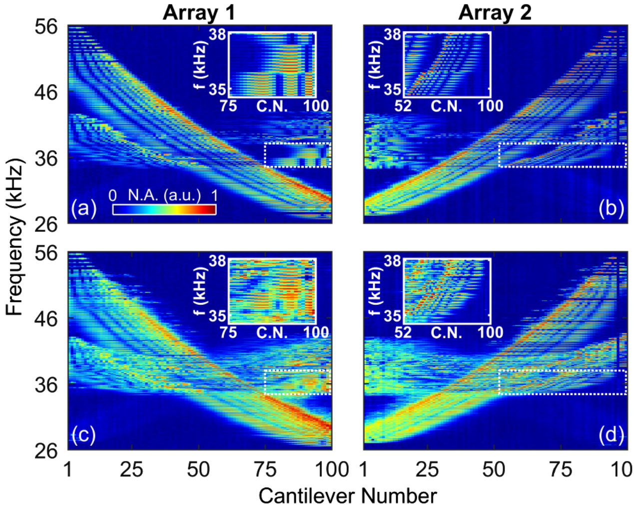

FIG. 3. The down-chirped frequency response at $\hat{V}_{ac} \approx 56$ V for (a) array 1 and (b) array 2 showing the emergence of a NPR band spanning across all cantilever numbers (C.N.). The insets highlight 22 NPR modes. Nonlinearities start to influence the dynamics significantly at $\hat{V}_{ac} \approx 81$ V as presented in (c) and (d) for array 1 and array 2, respectively. All plots are normalized independently and use the same normalized amplitude (N.A.) colormap.

To explain the dynamics more rigorously, a reduced-order (RO) model was developed using the Galerkin decomposition under the direction of Euler-Bernoulli beam theory [26,43]. Full details of the RO model are described in the Supplemental Material [44]. Numerical solutions were generated by solving the RO model's system of equations describing the dynamics of each individual beam using Runge-Kutta methods. As shown in Fig. 4(a), the simulated modal patterns qualitatively display many of the observed experimental features. Additional analysis on the spatial and temporal dynamics of the arrays using the RO model and spectral analysis further confirmed NPR actuation within our system. Power spectral densities using Welch's method were calculated for each frequency step in the numerical solution and concatenated together to form spectrograms. Whereas cantilevers near the center of the arrays were principally driven by fundamental parametric resonance within the NPR band, cantilevers near the periphery of the arrays were excited strictly by NPR within the NPR band and followed the relation $f_D \approx (f_j^{NM} + f_l^{NM})/2$ for the jth and lth modes as indicated by the responses of beams 10 and 11 in Figs. 4(b)–4(d). A similar analysis was performed on other adjacent beams within the arrays, and this provided further confirmation that the excitation of the beams outside of the spatially confined normal modes in the NPR band was principally due to the NPR mechanism.

In this Letter, we have demonstrated NPR excitation in large arrays of coupled, interdigitated MEMS cantilevers. The distinctive device topology produced spatially

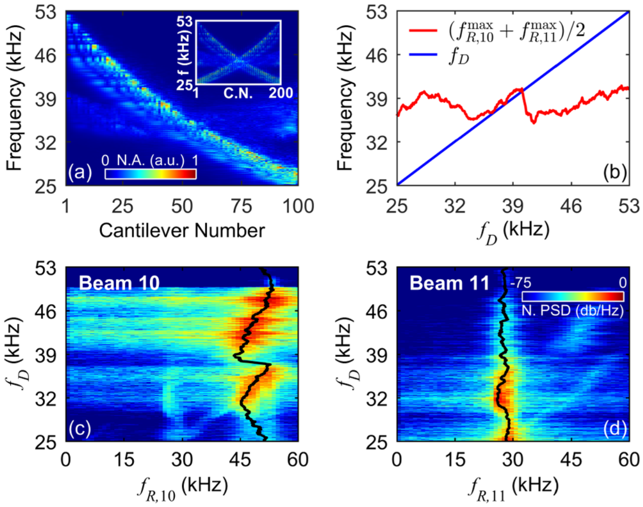

FIG. 4. (a) The calculated down-chirped frequency response of array 1 with $\hat{V}_{ac} = 100$ V showing a NPR band from ≈33 to ≈40 kHz. The inset depicts the response of both arrays. (b) Summation of the numerically calculated peak frequency response for beams 10 and 11. Within the NPR region, the summed peak frequency response of beam 10, $f_{R,10}^{\max}$, and beam 11, $f_{R,11}^{\max}$, follow the relation $f_D \approx (f_{R,10}^{\max} + f_{R,11}^{\max})/2$. The spectrograms of (c) beam 10 and (d) beam 11 computed using Welch's power spectral density (PSD) method along with the associated 9 point moving-average filtered peak frequency response shown as black lines. Both plots use the same normalized PSD colormap.

confined mode structures with mode-to-mode coupling between opposing arrays, which permitted efficient NPR actuation within the NPR frequency band. Exploiting NPR in future engineered M/NEMS could facilitate device operation at a multitude of frequencies, possibly enabling bandwidth expansion through frequency conversion and greater tunability of M/NEMS devices for applications such as resonance-based sensing. Furthermore, these arrays could potentially be utilized as a nondegenerate parametric amplifier by applying a small signal at f_j^{NM} to one array while pumping at $f_D \approx (f_j^{NM} + f_l^{NM})/2$ on the opposing array leading to signal amplification and phase noise reduction [45]. The high sensitivity of these coupled arrays to environmental perturbations will likely open new and interesting sensing scenarios based on NPR-actuated collective pattern recognition rather than on the frequency monitoring of individual elements.

This Letter was performed in part at the Physical Measurement Laboratory and the Center for Nanoscale Science and Technology at the National Institute of Standards and Technology and the Cornell NanoScale Facility, a member of the National Nanotechnology Coordinated Infrastructure, which is supported by the National Science Foundation (Grant No. NNCI-1542081). This Letter was partially supported by the National Science Foundation (Grant No. CMMI 1634664). Sandia National Laboratories is a multimission laboratory managed and operated by National Technology and Engineering Solutions of Sandia, LLC, a wholly owned subsidiary of Honeywell International Inc., for the U.S. Department of Energy's National Nuclear Security Administration under Award No. DE-NA0003525. S. K. acknowledges support from the Henry and Dinah Krongold Chair of Microelectronics. C. B. W. and R. D. A. acknowledge support under the Cooperative Research Agreement between the University of Maryland and the National Institute of Standards and Technology Center for Nanoscale Science and Technology, Grant No. 70NANB14H209, through the University of Maryland. This Letter describes objective technical results and analysis. Any subjective views or opinions that might be expressed in the Letter do not necessarily represent the views of the U.S. Department of Energy or the U.S. Government.

---

[*] robert.ilic@nist.gov

[1] E. Buks and M. L. Roukes, J. Microelectromech. Syst. **11**, 802 (2002).

[2] M. Sato, B. E. Hubbard, A. J. Sievers, B. Ilic, D. A. Czaplewski, and H. G. Craighead, Phys. Rev. Lett. **90**, 044102 (2003).

[3] M. Sato, B. E. Hubbard, and A. J. Sievers, Rev. Mod. Phys. **78**, 137 (2006).

[4] E. Kenig, B. A. Malomed, M. C. Cross, and R. Lifshitz, Phys. Rev. E **80**, 046202 (2009).

[5] R. Lifshitz and M. C. Cross, Phys. Rev. B **67**, 134302 (2003).

[6] M. C. Cross, J. L. Rogers, R. Lifshitz, and A. Zumdieck, Phys. Rev. E **73**, 036205 (2006).

[7] S.-B. Shim, M. Imboden, and P. Mohanty, Science **316**, 95 (2007).

[8] D. K. Agrawal, J. Woodhouse, and A. A. Seshia, J. Appl. Phys. **115**, 164904 (2014).

[9] C. T.-C. Nguyen, IEEE Trans. Ultrason. Ferroelectrics Freq. Control **54**, 251 (2007).

[10] K. R. Qalandar, B. S. Strachan, B. Gibson, M. Sharma, A. Ma, S. W. Shaw, and K. L. Turner, Appl. Phys. Lett. **105**, 244103 (2014).

[11] H.-C. Chang, X. Cao, U. K. Mishra, and R. A. York, IEEE Trans. Microwave Theory Tech. **45**, 604 (1997).

[12] M. H. Matheny, M. Grau, L. G. Villanueva, R. B. Karabalin, M. C. Cross, and M. L. Roukes, Phys. Rev. Lett. **112**, 014101 (2014).

[13] M. Zhang, S. Shah, J. Cardenas, and M. Lipson, Phys. Rev. Lett. **115**, 163902 (2015).

[14] F. Torres, A. Uranga, M. Riverola, G. Sobreviela, and N. Barniol, Sensors **16**, 1690 (2016).

[15] M. Spletzer, A. Raman, A. Q. Wu, X. Xu, and R. Reifenberger, Appl. Phys. Lett. **88**, 254102 (2006).

[16] M. Spletzer, A. Raman, H. Sumali, and J. P. Sullivan, Appl. Phys. Lett. **92**, 114102 (2008).

[17] P. Thiruvenkatanathan, J. Yan, J. Woodhouse, A. Aziz, and A. A. Seshia, Appl. Phys. Lett. **96**, 081913 (2010).

[18] C. Zhao, M. H. Montaseri, G. S. Wood, S. H. Pu, A. A. Seshia, and M. Kraft, Sens. Actuators A **249**, 93 (2016).

[19] M. Sato, B. E. Hubbard, L. Q. English, A. J. Sievers, B. Ilic, D. A. Czaplewski, and H. G. Craighead, Chaos **13**, 702 (2003).

[20] M. Sato and A. J. Sievers, Phys. Rev. Lett. **98**, 214101 (2007).

[21] T. Ono, K. Tanno, and Y. Kawai, J. Micromech. Microeng. **24**, 025012 (2014).

[22] M. Zhang, G. S. Wiederhecker, S. Manipatruni, A. Barnard, P. McEuen, and M. Lipson, Phys. Rev. Lett. **109**, 233906 (2012).

[23] M. Bagheri, M. Poot, L. Fan, F. Marquardt, and H. X. Tang, Phys. Rev. Lett. **111**, 213902 (2013).

[24] E. Gil-Santos, M. Labousse, C. Baker, A. Goetschy, W. Hease, C. Gomez, A. Lemaître, G. Leo, C. Ciuti, and I. Favero, Phys. Rev. Lett. **118**, 063605 (2017).

[25] P. Thiruvenkatanathan, J. Yan, J. Woodhouse, and A. A. Seshia, J. Microelectromech. Syst. **18**, 1077 (2009).

[26] S. Krylov, S. Lulinsky, B. R. Ilic, and I. Schneider, Appl. Phys. Lett. **105**, 071909 (2014).

[27] P. N. Kambali, G. Swain, A. K. Pandey, E. Buks, and O. Gottlieb, Appl. Phys. Lett. **107**, 063104 (2015).

[28] M. C. Cross, A. Zumdieck, R. Lifshitz, and J. L. Rogers, Phys. Rev. Lett. **93**, 224101 (2004).

[29] J. F. Rhoads, S. W. Shaw, and K. L. Turner, J. Dyn. Syst., Meas., Control **132**, 034001 (2010).

[30] P. Cudmore and C. A. Holmes, Chaos **25**, 023110 (2015).

[31] A. H. Nayfeh and D. T. Mook, *Nonlinear Oscillations* (Wiley, New York, 2008).

[32] K. L. Turner, S. A. Miller, P. G. Hartwell, N. C. MacDonald, S. H. Strogatz, and S. G. Adams, Nature (London) **396**, 149 (1998).

[33] Y. Jia, S. Du, and A. A. Seshia, Sci. Rep. **6**, 30167 (2016).

[34] A. H. Nayfeh and D. T. Mook, J. Acoust. Soc. Am. **62**, 375 (1977).

[35] A. A. Mailybayev and A. P. Seyranian, J. Appl. Math. Mech. **65**, 755 (2001).

[36] R. Baskaran and K. L. Turner, J. Micromech. Microeng. **13**, 701 (2003).

[37] M. Napoli, W. Zhang, K. Turner, and B. Bamieh, J. Microelectromech. Syst. **14**, 295 (2005).

[38] H. Okamoto, A. Gourgout, C.-Y. Chang, K. Onomitsu, I. Mahboob, E. Y. Chang, and H. Yamaguchi, Nat. Phys. **9**, 480 (2013).

[39] I. Mahboob, H. Okamoto, K. Onomitsu, and H. Yamaguchi, Phys. Rev. Lett. **113**, 167203 (2014).

[40] Y. S. Patil, S. Chakram, L. Chang, and M. Vengalattore, Phys. Rev. Lett. **115**, 017202 (2015).

[41] S. Cho, S. U. Cho, M. Jo, J. Suh, H. C. Park, S. G. Kim, S.-B. Shim, and Y. D. Park, Phys. Rev. Applied **9**, 064023 (2018).

[42] Y. Linzon, B. Ilic, S. Lulinsky, and S. Krylov, J. Appl. Phys. **113**, 163508 (2013).

[43] N. Dick, S. Grutzik, C. B. Wallin, B. R. Ilic, S. Krylov, and A. T. Zehnder, J. Vib. Acoust. **140**, 051013 (2018).

[44] See Supplemental Material at http://link.aps.org/supplemental/10.1103/PhysRevLett.121.264301 for additional details regarding the RO model, the FE model, and the numerical calculations. Further experimental results showing hysteresis and the device response to piezoelectric drive can also be found in the Supplemental Material.

[45] A. Olkhovets, D. W. Carr, J. M. Parpia, and H. G. Craighead, in *Proceedings of the 14th IEEE International Conference on Micro Electro Mechanical Systems Technical Digest, MEMS, 2001* (2001), pp. 298–300, DOI: 10.1109/MEMSYS.2001.906537.

Supplemental Material for "Nondegenerate Parametric Resonance in Large Ensembles of Coupled Micromechanical Cantilevers with Varying Natural Frequencies"

Christopher B. Wallin,[1,2] Roberto De Alba,[1,2] Daron Westly,[1]
Glenn Holland,[1] Scott Grutzik,[3] Richard H. Rand,[4,5] Alan T.
Zehnder,[4] Vladimir A. Aksyuk,[1] Slava Krylov,[6] and B. Robert Ilic[1,*]

[1]*Physical Measurement Laboratory, National Institute of Standards and Technology, Gaithersburg, MD 20899, USA*

[2]*Institute for Research in Electronics and Applied Physics, University of Maryland, College Park, MD 20742, USA*

[3]*Component Science and Mechanics, Sandia National Laboratories, Albuquerque, NM 87185, USA*

[4]*Sibley School of Mechanical and Aerospace Engineering, Cornell University, Ithaca, NY 14853, USA*

[5]*Department of Mathematics, Cornell University, Ithaca, NY 14853, USA*

[6]*School of Mechanical Engineering, Faculty of Engineering, Tel Aviv University, Ramat Aviv 69978, Tel Aviv, Israel*

(Dated: December 12, 2018)

FORMULATION

Cantilever Array Model

The cantilever array model developed herein assumes that the vibrational motion of the n^{th} individual cantilever is governed by Euler-Bernoulli theory. The rotational and axial inertia of each beam is presumed insignificant relative to the its transverse inertia [1]. The model does, however, incorporate geometric nonlinearities that are the result of large beam deflections [2]. These geometric nonlinearities are the only on-site nonlinearity and will produce a Duffing-type nonlinear term in the subsequently derived reduced order (RO) model equations. Additionally, in accordance with the design and layout of the array, the cantilever array model has a nearest-neighbor coupling term due to the fringing electrostatic fields produced by the applied voltage. In order to effectively account for this coupling, a simplified model of the fringing fields with a closed-form approximate expression for the generated electrostatic force is employed. The approximate expression for the electrostatic force per unit length is given by [3, 4]

$$F_n^e = \alpha\sigma\hat{V}^2\left(\frac{\frac{\hat{w}_{n+1}-\hat{w}_n}{h}}{1+\sigma|\frac{\hat{w}_{n+1}-\hat{w}_n}{h}|^{2p}} - \frac{\frac{\hat{w}_n-\hat{w}_{n-1}}{h}}{1+\sigma|\frac{\hat{w}_n-\hat{w}_{n-1}}{h}|^{2p}}\right)H(\hat{y}_n-\hat{y}_n^e), \tag{S.1}$$

where $\hat{w}_n(\hat{y}_n)$ is the out-of-plane defection of the n^{th} beam, $\hat{y}_n$ is the coordinate along the n^{th} beam's longitudinal axis, $\hat{y}_n^e = L_n - L_e$ defines the start of the overlap region for the n^{th} beam, h is the thickness of the beam, and $\hat{V}(\hat{t})$ is the time dependent voltage. The remaining terms in Eq. (S.1) are geometry dependent fitting parameters and have to be calculated numerically. For the given device geometry, we find $\alpha = 2.45 \times 10^{-6}$ N $\cdot$ mV $^{-2}$, $\sigma = 0.133$, and $p = 1.191$. Furthermore, since the electrostatic interaction force occurs only in the overlap region defined by L_e, the electrostatic coupling force is weighted by the Heaviside step function, $H(\hat{y}_n - \hat{y}_n^e)$. Additional details of the fringing field model can be found in [3, 4].

Therefore, with these assumptions, the equation of motion of the n^{th} beam ($n = 1, 2, \ldots, 200$) is given by

$$\rho A\frac{\partial^2\hat{w}_n}{\partial\hat{t}^2} + \hat{c}_o\frac{\partial\hat{w}_n}{\partial\hat{t}} + EI\frac{\partial^4\hat{w}_n}{\partial\hat{y}_n^4} + EI\frac{\partial}{\partial\hat{y}_n}\left[\frac{\partial\hat{w}_n}{\partial\hat{y}_n}\frac{\partial}{\partial\hat{y}_n}\left(\frac{\partial\hat{w}_n}{\partial\hat{y}_n}\frac{\partial^2\hat{w}_n}{\partial\hat{y}_n^2}\right)\right] - \alpha\sigma\hat{V}^2\left(\frac{\frac{\hat{w}_{n+1}-\hat{w}_n}{h}}{1+\sigma\,|\frac{\hat{w}_{n+1}-\hat{w}_n}{h}|^{2p}} - \frac{\frac{\hat{w}_n-\hat{w}_{n-1}}{h}}{1+\sigma|\frac{\hat{w}_n-\hat{w}_{n-1}}{h}|^{2p}}\right)H(\hat{y}_n-\hat{y}_n^e) = \rho A\frac{\partial^2\hat{z}_B}{\partial\hat{t}^2}. \tag{S.2}$$

Here $A = bh$ and $I = bh^3/12$ are the area and the second moment of area of the rectangular cross-section of the beam of width b and thickness h, and $\hat{c}_o$ is the coefficient on-site linear viscous damping, which is inversely related to the quality factor of the beam, Q. The material parameters are $E = 169$ GPa and $\rho = 2300$ kg/m^3, which are the Young's modulus and the density of silicon, respectively. The right side of Eq. (S.2) describes a uniformly distributed force acting on the beam through a forced excitation of the substrate which experimentally could be realized using piezoelectric actuation. This force is specified by using the out-of-plane spatial coordinate $\hat{z}_B$.

In order to solve Eq. (S.2), appropriate boundary conditions must considered at the free and clamped ends of each of the beams. At the free end of the beams where $\hat{y}_n = L_n$, the boundary conditions are given by $EI(\partial^2 \hat{w}_n/\partial^2 \hat{y}_n) = 0$ and $EI(\partial^3 \hat{w}_n/\partial^3 \hat{y}_n) = 0$. At the clamped end of the beams where $\hat{y}_n = 0$, the situation is not as straightforward since the clamping is nonideal due to the overhang. The nonideal clamping of the overhang decreases the natural frequencies of the eigenmodes relative to ideal clamping and produces long range mechanical coupling between the cantilevers which was not considered in Eq. (S.2) [1]. At this point in model development, the on-site terms will assume ideal clamping to the overhang and the mechanical coupling will be directly implemented into the RO model with the mechanical coupling matrix determined by finite element (FE) analysis [5].

To proceed, Eq. (S.2) is nondimensionalized resulting in the expression given by

$$\frac{\partial^2 w_n}{\partial t^2} + c_o \frac{\partial w_n}{\partial t} + \omega_n^2 \frac{\partial^4 w_n}{\partial y^4} + \tilde{\varepsilon}\omega_n^3 \frac{\partial}{\partial y}\left[\frac{\partial w_n}{\partial y}\frac{\partial}{\partial y}\left(\frac{\partial w_n}{\partial y}\frac{\partial^2 w_n}{\partial y^2}\right)\right] - \tilde{\beta}V^2\left(\frac{(w_{n+1} - w_n)}{1+\sigma\left|w_{n+1} - w_n\right|^{2p}} - \frac{(w_n - w_{n-1})}{1+\sigma\left|w_n - w_{n-1}\right|^{2p}}\right) H(y - y_n^e) = -\frac{\partial^2 z_B}{\partial t^2}. \quad \text{(S.3)}$$

The nondimensional parameters used in Eq. (S.3) are shown in Table S.I. Here, V_0 is the reference voltage taken to be the unit voltage, and L_0 is the reference length taken to be L_{max}.

Reduced Order Model

In order to reduce the computational complexity of the problem while retaining the leading dynamical phenomena of the cantilever array system, a RO model based on the Galerkin decomposition will be formulated using the eigenmodes of an ideally clamped cantilever as

TABLE S.I. Nondimensional parameters used in Eq. (S.3).

Quantity	**Description**
$y = \hat{y}_n/L_n$	Coordinate along the n^{th} beam
$t = \hat{t}\sqrt{EI/(\rho A L_0^4)}$	Time
$w_n(y,t) = \hat{w}_n(\hat{y},\hat{t})/h$	Deflection of the n^{th} beam
$g = \hat{g}/h$	Distance between the beams
$c_o = \hat{c}_o\sqrt{L_0^4/(EI\rho A)}$	OS damping parameter
$\tilde{\varepsilon} = (h/L_0)^2$	Aspect ratio parameter
$\omega_n = (L_0/L_n)^2$	Length ratio parameter
$\tilde{\beta} = \alpha\sigma L_{max}^4 V_0^2/(EIh)$	Voltage parameter

basis functions. While a brute-force full-scale FE analysis with the included nonlinear electrostatic forces would be optimal, extensive computational resources are necessary in order to appropriately address the large degree of freedom system along with all of its nonlinearities. Accordingly, taking the more pedestrian approach, the out-of-plane deflection of the n^{th} beam can be approximated by a single degree of freedom expression given by

$$w_n(y,t) \approx q_n(t)\,\phi_1(y), \tag{S.4}$$

where $q_n(t)$ serves as a generalized coordinate and $\phi_1(y)$ is the fundamental eigenmode of a linear, undamped, ideally clamped cantilever given by the expression [6]

$$\phi_1(y) = C_1\left[\sin(\lambda_1 y) - \sinh(\lambda_1 y) - \frac{(\sin(\lambda_1)+\sinh(\lambda_1))(\cos(\lambda_1 y)-\cosh(\lambda_1 y))}{\cos(\lambda_1)+\cosh(\lambda_1)}\right]. \tag{S.5}$$

Here, $\lambda_1 = 1.875$ is the fundamental eigenvalue of an ideally clamped cantilever. The normalization constant $C_1 = 0.367$ is chosen such that $\max\limits_{0\le y\le 1}\phi_1(y) = 1$. The eigenmode given by Eq. (S.5) is the solution to the eigenvalue problem related to Eq. (S.3) with $c_o = 0$, $\tilde{\varepsilon} = 0$, $\tilde{\beta} = 0$, and $\partial^2 z_B/\partial t^2 = 0$.

Applying the Galerkin methodology by inserting Eq. (S.4) into Eq. (S.3) and integrating over the beam length produces a system of coupled, nonlinear ordinary differential equations. However, these equations still lack the mechanical coupling due to the compliant overhang and must be amended by adding a term involving a linear coupling matrix. This coupling matrix will have a considerable number of off-diagonal coefficients being nonzero since the mechanical coupling in the device is nonlocal. Moreover, by only adding a linear coupling matrix, it has been explicitly assumed that the overhang inertia and any nonlinear elastic coupling is negligible in the model. Thus, the governing equations for the model become

$$m\ddot{q}_n + c_o m\dot{q}_n + k_o\omega_n^2 q_n + \tilde{\varepsilon}\omega_n^3 k_o^{nl} q_n^3 - \sum_s k_{ns}q_s - \tilde{\beta}V^2\left(\int\limits_{y_n^e}^{1}\frac{(q_{n+1}-q_n)\phi_1^2}{1+\sigma\left|(q_{n+1}-q_n)\phi_1\right|^{2p}}\,dy - \int\limits_{y_n^e}^{1}\frac{(q_n-q_{n-1})\phi_1^2}{1+\sigma\left|(q_n-q_{n-1})\phi_1\right|^{2p}}\,dy\right) = -\ddot{z}_B a, \quad \text{(S.6)}$$

where

$$k_o = \int\limits_0^1 (\phi_1'')^2\,dy, \quad k_o^{nl} = 2\int\limits_0^1 (\phi_1')^2(\phi_1'')^2\,dy, \quad m = \int\limits_0^1 \phi_1^2\,dy, \quad a = \int\limits_0^1 \phi_1\,dy. \quad \text{(S.7)}$$

Here, $\dot{q}_n$ and $\ddot{q}_n$ are the first and second time derivatives of q_n. Similarly, ϕ_1' and ϕ_1'' correspond to the first and second spatial derivatives of the given basis function. Using the basis given in Eq. (S.5), the integrals in Eq. (S.7) can be numerically evaluated and are found to be $k_o = 3.091$, $k_o^{nl} = 2.527$, $m = 0.25$, and $a = 0.391$. The coefficients k_o and k_o^{nl} are related to the linear and nonlinear on-site bending stiffness of the cantilever, and m is related to the mass of the cantilever. Additionally, using these coefficients, we find that the nondimensional fundamental frequency of the ideally clamped cantilever is $\sqrt{k_o/m} = \omega_0 = \lambda_1^2 = 3.516$.

The integrals involving the calculation of electrostatic force in Eq. (S.6) cannot be evaluated in closed form. Numerical evaluation of Eq. (S.6) requires that these integrals be computed at each time step which greatly increases the total simulation time. Thus, we assume that $\phi_1(y) \approx 1$ in the denominator of the Eq. (S.6) integrands. This enables the integrals to be put in algebraic form which markedly simplifies the simulation. Therefore, we have

$$m\ddot{q}_n + c_o m\dot{q}_n + k_o\omega_n^2 q_n + \tilde{\varepsilon}\omega_n^3 k_o^{nl} q_n^3 - \sum_s k_{ns}q_s - \tilde{\beta}V^2 m_n^e\left(\frac{q_{n+1}-q_n}{1+\sigma\left|q_{n+1}-q_n\right|^{2p}} - \frac{q_n-q_{n-1}}{1+\sigma\left|q_n-q_{n-1}\right|^{2p}}\right) = -\ddot{z}_B a, \quad \text{(S.8)}$$

where m_n^e is defined by

$$m_n^e = \int\limits_{y_n^e}^{1} \phi_1^2\,dy. \quad \text{(S.9)}$$

TABLE S.II. Non-dimensional quantities used in Eq. (S.10).

Quantity	**Description**
$\tau = t\omega_0$	Time
$u_n = q_n \sqrt[2p]{\sigma}$	Deflection of the n^{th} mass
$u_B = z_B \sqrt[2p]{\sigma}$	Deflection of the base
$\mu_n = m_n^e/m$	Mass ratio
$\varepsilon = \tilde{\varepsilon} k_o^{nl}/(k_o \sqrt[p]{\sigma})$	Nonlinear OS stiffness parameter
$\beta = \tilde{\beta}/\omega_0^2$	Voltage parameter
$\gamma = a/m$	Base acceleration parameter

Here, the non-dimensional boundary location defining the overlap region, y_n^e, is given by $y_n^e = (L_n - L_e)/L_n$. Dividing Eq. (S.8) by m along with rescaling time by $\tau = t\omega_0$ and the deflections by $q_n = u_n/\sqrt[2p]{\sigma}$ and $z_B = u_B/\sqrt[2p]{\sigma}$ gives

$$\ddot{u}_n + Q^{-1}\dot{u}_n + \omega_n^2 u_n + \varepsilon \omega_n^3 u_n^3 - \sum_s k_{ns} u_s - \\ \beta \mu_n V^2 \left(\frac{u_{n+1} - u_n}{1 + |u_{n+1} - u_n|^{2p}} - \frac{u_n - u_{n-1}}{1 + |u_n - u_{n-1}|^{2p}} \right) = -\gamma \ddot{u}_B, \quad \text{(S.10)}$$

where the over-dot is redefined as the partial derivative with respect to τ. Table S.II gives the non-dimensional parameters used in Eq. (S.10).

Finite Element Model

Proper evaluation of the k_{ns} stiffness coefficients found in Eq. (S.10) requires a full-scale three-dimensional finite element (FE) analysis [5]. The FE model was implemented using two distinct meshes. The overhang mesh was composed of two-dimensional 8-node shell elements with quadratic interpolating functions in each orthogonal direction. The beam mesh was formulated using 2-node multi degree of freedom elements with a rectangular cross-section and constant mass representation. The number of degrees of freedom for each beam element varied depending on the length of the beam.

The eigenvectors and eigenfrequencies of the array were directly determined from the FE solutions. From the generated eigenvectors and their associated nodal displacements, sub-sets $\tilde{\boldsymbol{\psi}}^{(\boldsymbol{k})}$ were assembled such that $\tilde{\boldsymbol{\psi}}^{(\boldsymbol{k})}$ describes the free-end displacement of the cantilevers for the k^{th} eigenvector where $k = 1, 2, \dots 100$. Since the numerically derived FE eigenvectors are not exactly orthogonal, Gram-Schmidt orthogonalization was performed before modal matrix construction. The modal matrix given by

$$\tilde{\mathbf{\Psi}} = \left[\tilde{\boldsymbol{\psi}}^{\mathbf{(1)}}, \tilde{\boldsymbol{\psi}}^{\mathbf{(2)}}, \dots, \tilde{\boldsymbol{\psi}}^{\mathbf{(100)}}\right] \tag{S.11}$$

was normalized by employing the orthogonality with respect to the unit mass matrix giving

$$\mathbf{\Psi} = \frac{\tilde{\mathbf{\Psi}}}{\sqrt{\tilde{\mathbf{\Psi}}^T \tilde{\mathbf{\Psi}}}}. \tag{S.12}$$

From the normalized modal matrix, the k_{ns} coefficients were extracted using the stiffness matrix orthogonality relation,

$$\mathbf{\Psi}^T \mathbf{K} \mathbf{\Psi} = \mathbf{\Lambda}, \tag{S.13}$$

where $\mathbf{\Lambda} = \left[\lambda^{(k)} \delta_{km}\right]$ is a diagonal matrix with $\lambda^{(k)} = \lambda^{(k)}_{FE} / \lambda^{(1)}_{FE}$ being the normalized FE eigenvalues which range from 1.00 to approximately 2.22. Explicitly, the stiffness matrix which contains both onsite and intersite terms can be written in terms of the normalized eigenvectors and eigenvalues as

$$\mathbf{K} = \left(\mathbf{\Psi}^T\right)^{-1} \mathbf{\Lambda} \mathbf{\Psi}^{-1}. \tag{S.14}$$

The symmetric stiffness matrix generated from the FE analysis has the form

$$\mathbf{K} = \begin{pmatrix} 1.21516 & 0 & -0.00064 & 0 & -0.00017 & 0 & \dots \\ 0 & 4.92888 & 0 & -0.00258 & 0 & -0.00052 & \dots \\ -0.00064 & 0 & 1.12156 & 0 & -0.03095 & 0 & \dots \\ 0 & -0.00258 & 0 & 4.27827 & 0 & -0.15835 & \dots \\ -0.00017 & 0 & -0.03095 & 0 & 1.11243 & 0 & \dots \\ 0 & -0.00052 & 0 & -0.15835 & 0 & 4.08203 & \dots \\ \vdots & \vdots & \vdots & \vdots & \vdots & \vdots & \ddots \end{pmatrix}. \tag{S.15}$$

MODAL OVERLAP AND NPR BAND FORMATION

The eigenfrequencies and eigenmodes determined from the FE analysis can be used to demonstrate why NPR exists only in a specific frequency band in addition to its concavity. Obviously, a necessary condition for NPR development is that the modes have to spatially overlap to enable coupling between the modes. Due to the localized nature of the modes in the device, only certain modes will interact with one another. In order to give a quantitative estimate of the degree of coupling between modes, overlap summations were calculated using the absolute value of the normalized amplitudes of the j^{th} and l^{th} eigenmodes derived from FE analysis for $j, l = 1, 2, \ldots 100$. More specifically, the overlap summation for the j^{th} and l^{th} normalized eigenmodes is given by

$$\zeta^{(j),(l)} = \sum_{n=1}^{100} |\psi_n^{(j)}||\psi_{101-n}^{(l)}|. \tag{S.16}$$

These overlaps generally exist in neighborhoods such that $l \approx 100 - j$ due to the geometry of the device. A second necessary condition for NPR is that $f_D \approx (f_j^{NM} + f_l^{NM})/2$. As shown in Fig. S.1(b), these two necessary conditions for NPR exist solely within a band from $f_j^{NM} + f_l^{NM} \approx 66$ kHz to $f_j^{NM} + f_l^{NM} \approx 80$ kHz which corresponds to drive frequencies from ≈ 33 kHz to ≈ 40 kHz. This result matches the simulation results and coincides closely with the experimental results. Moreover, due to the shape of eigenfrequency distribution,

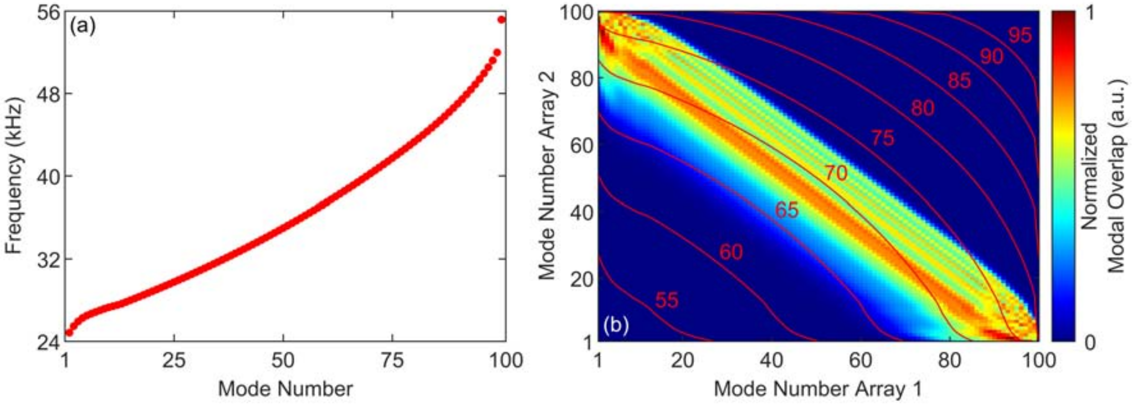

FIG. S.1. (a) Eigenfrequencies calculated using FE analysis. (b) Normalized modal overlap between modes on opposing arrays illustrating where NPR could be generated for a given frequency. The contour lines correspond to the sum of eigenfrequencies $f_j^{NM} + f_l^{NM}$ for the j^{th} mode number from Array 1 and the l^{th} mode number from Array 2. The contour frequency values are in kHz. NPR will arise in regions of significant modal overlap with the necessary condition of $f_D \approx (f_j^{NM} + f_l^{NM})/2$. Due to the specific curvature of the contours, modes excited near the periphery of the device have modal overlap at larger summed eigenfrequency values which gives the characteristic concave-up profile to the NPR band.

the NPR bandwidth is spatially nonuniform with shifts to higher frequencies near the edge of the device creating a concave-up NPR band. This is explicitly shown in Fig. S.1.

SPECTROGRAM CALCULATIONS

Eq. (S.10) was solved numerically using Runge-Kutta methods with 500 frequency steps. For each frequency step, a temporal discretization of 80×10^3 time steps was appropriated to effectively average out any transient behavior due to initial conditions. The deflection time series of individual beams was used to compute the power spectral density (PSD) using Welch's method [7] with a Hann window at each frequency step. Each PSD was then compiled together to produce the spectrograms. Using the PSDs, the peak frequency response for the j^{th} beam was determined at each frequency step. To reduce noise, a 9 point moving average filter was applied to the peak frequency response curve, and the samples were appropriately shifted by 4 samples to account for the filter delay.

HYSTERESIS

The observed modal patterns were highly dependent on the voltage sweep direction which is a consequence of the nonlinearities in the cantilever array. For example, Fig. S.2 shows that the device response appeared generally stronger, broader, and more pronounced for the down-chirped drive relative to the up-chirped drive, thus demonstrating that the array has a dominant softening nonlinearity at high voltages. The source of the softening nonlinearity is the electrostatic coupling resulting from the functional form of Eq. (S.1). Previous experimental studies of similar devices have shown that the electrostatic nonlinearity is softening [3, 4] whereas the onsite and intersite elastic nonlinearity is hardening [1], thus suggesting that the electrostatic nonlinearity principally governs the nonlinear dynamics of the arrays at large drive voltages. Additionally, as a consequence of the softening nonlinearity in the system, only the down-chirped modal patterns exhibit full NPR band development whereby the cantilevers oscillate via NPR across the whole array. The down-chirped NPR band has a slight concave up profile illustrating that the NPR typically initiates near the perimeter of the device. The concave up band profile is the result of the specific distribution of the eigenfrequencies along with the spatial locations of the modes as previously discussed. The

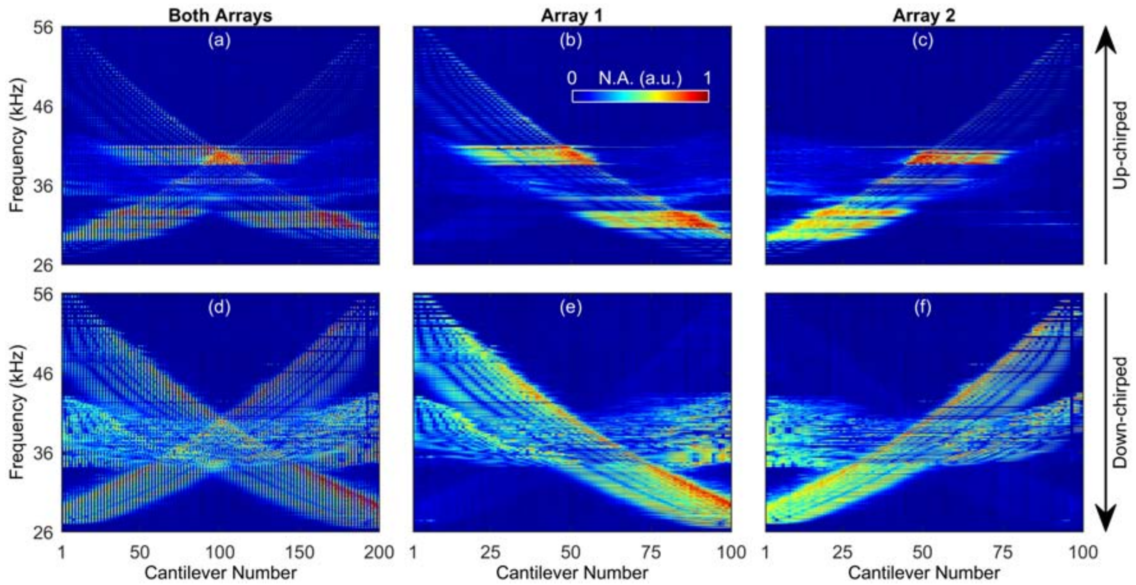

FIG. S.2. Up-chirped frequency response measurements at $\hat{V}_{ac} \approx 68$ V showing the response of (a) both arrays, (b) Array 1, and (c) Array 2. Down-chirped frequency response measurements at $\hat{V}_{ac} \approx 68$ V showing the response of (d) both arrays, (e) Array 1, and (f) Array 2. Hysteresis due to the softening nonlinearity is readily apparent as the down-chirped response is generally stronger, exhibits broader resonant peaks, and generates significantly more NPR compared to the up-chirped response. All plots are normalized independently and follow the same normalized amplitude (N.A.) colormap.

up-swept modal patterns also display interesting features including large amplitude bands which are broad compared to mode spacing, but the response appears to have minimal NPR and generally follows the eigenmode shapes predicted by FE analysis.

To demonstrate the softening nonlinearity more explicitly, we performed further experiments at a significantly higher frequency resolution by performing frequency sweeps at a rate of ≈ 10 Hz/s. Figure S.3 shows the down-chirped frequency response from ≈ 30 kHz to ≈ 29.2 kHz at a drive voltage of $\hat{V}_{ac} \approx 68$ V. Each of the 9 modes depicted clearly illustrate an asymmetric resonance peak with abrupt jumps on the lower frequency side. This is further evidence of the softening nonlinearity resulting from the electrostatic coupling within the device.

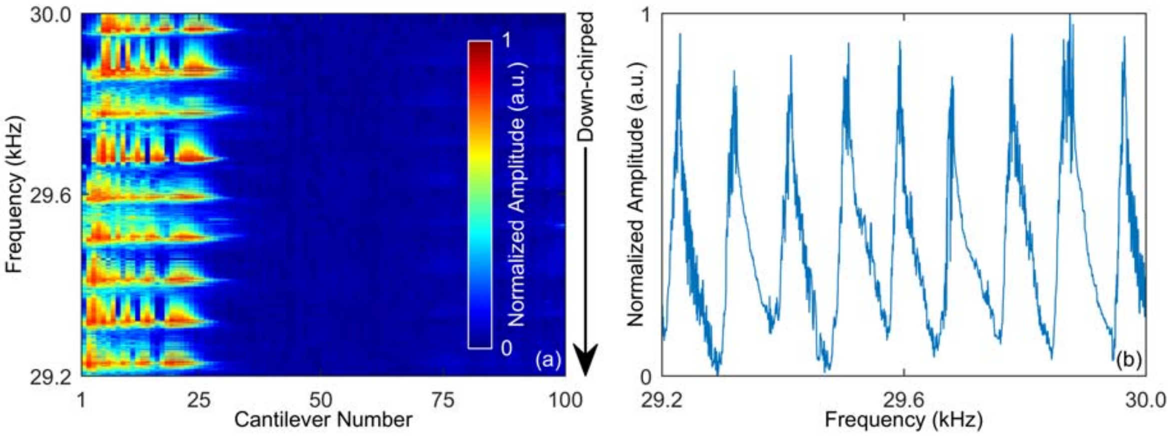

FIG. S.3. (a) The down-chirped frequency response at $\hat{V}_{ac} \approx 68$ V showing the softening nonlinear behavior of 9 modes. (b) The cantilever-averaged frequency response curve giving 9 asymmetric resonance peaks. All resonance peaks exhibit a jump phenomenon on the side of lower frequency, which is indicative of a softening nonlinearity. Both plots are normalized independently.

DEVICE RESPONSE WITH PIEZOELECTRIC DRIVE

To further confirm that NPR was driven by the electrostatic coupling, the arrays were also excited strictly by a piezoelectric transducer (PZT) as shown in FIG. S.4. The PZT harmonically accelerates the device in a spatially uniform manner providing a forced excitation to the cantilevers. PZT provides no parametric excitation.

The device was mounted on the PZT using vacuum grease in-between the substrate and PZT. The PZT response was driven using an arbitrary function generator since drive voltages no higher than ≈ 4.1 V were used. In order to try to generate NPR band formation, the cantilevers were driven up to the point of cantilever breakage as shown in Fig. S.4(b). Due to the removal of the softening nonlinearity provided by the electrostatic coupling, the up-chirped response was more intense relative to the down-chirped response. A very limited number of cantilevers responded outside of the normal mode shapes in narrow frequency bands for the up-chirped response whereas the down-chirped response showed essentially no deviations from the normal modes.

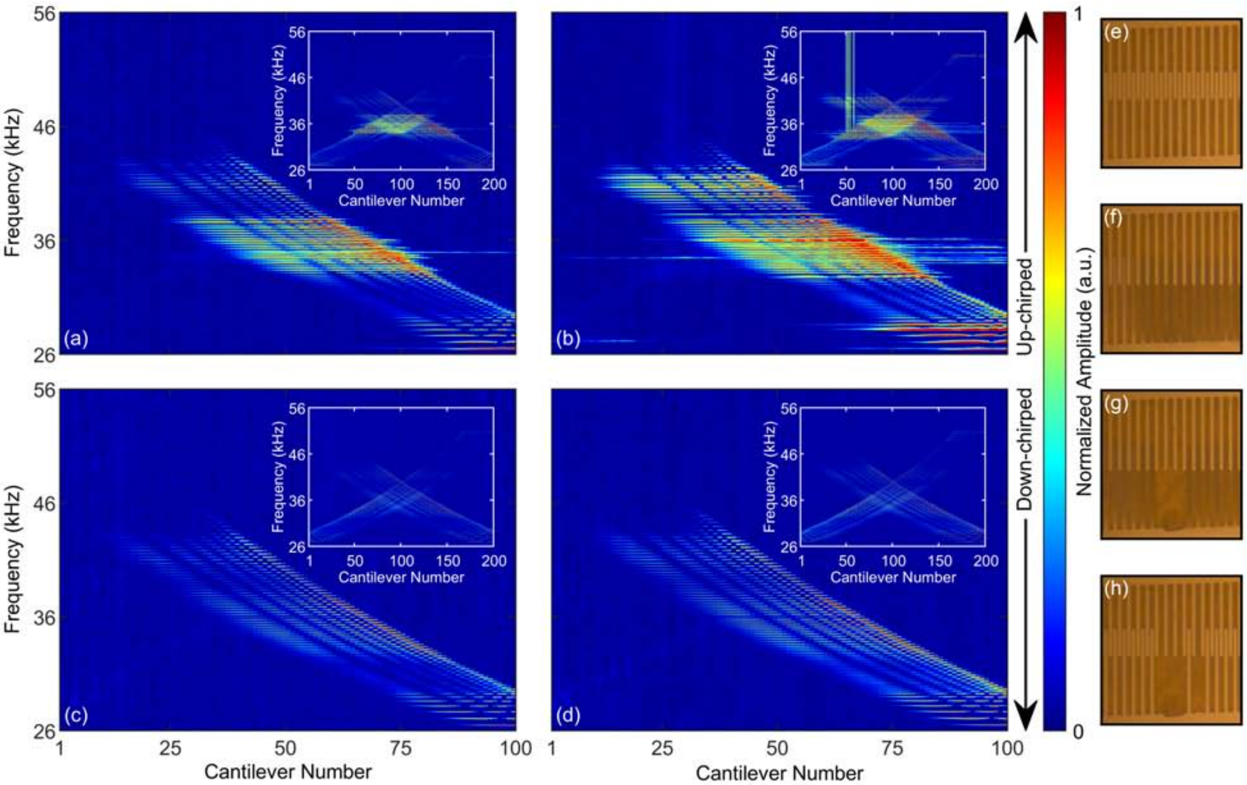

FIG. S.4. Frequency response measurements using a PZT at (a) $V \approx 2.7$ V and up-chirped drive, (b) $V \approx 4.1$ V and up-chirped drive, (c) $V \approx 2.7$ V and down-chirped drive, and (d) $V \approx 4.1$ V and down-chirped drive. Only responses of Array 1 are shown for clarity. The insets show both responses of Arrays 1 and 2 in a single plot. The inset in (b) shows the breakage of 4 cantilevers near cantilever 50 as indicted by the vertical lines. Micrographs showing the region of cantilever breakage at (e) $f_D \approx 26$ kHz, (f) $f_D \approx 33.8$ kHz and one frame prior to breakage, (g) $f_D \approx 33.8$ kHz and one frame after breakage, and (h) $f_D \approx 56$ kHz. All measurements were taken in vacuum at $\approx 10^{-3}$ Pa.

---

* robert.ilic@nist.gov

[1] M. Sato, B. E. Hubbard, and A. J. Sievers, Reviews of Modern Physics **78**, 137 (2006).

[2] M. R. M. Crespo da Silva and C. C. Glynn, Journal of Structural Mechanics **6**, 437 (1978).

[3] Y. Linzon, B. Ilic, S. Lulinsky, and S. Krylov, Journal of Applied Physics **113**, 163508 (2013).

[4] S. Krylov, S. Lulinsky, B. R. Ilic, and I. Schneider, Applied Physics Letters **105**, 071909 (2014).

[5] N. Dick, S. Grutzik, C. B. Wallin, B. R. Ilic, S. Krylov, and A. T. Zehnder, Journal of Vibration and Acoustics **140**, 051013 (2018).

[6] L. Meirovitch, *Fundamentals of Vibrations* (Waveland Press, 2010).

[7] P. Welch, IEEE Transactions on Audio and Electroacoustics **15**, 70 (1967).